Modern Applied Science; Vol. 12, No. 12; 2018
ISSN 1913-1844 E-ISSN 1913-1852
Published by Canadian Center of Science and Education

Electrical Conductivity Behavior of $La_{0.5}Ca_{0.5}Mn_{0.5}Fe_{0.5}O_3$ Synthetized by the Solid State Reaction

H. A. Martínez-Rodríguez[1], J.F. Jurado[2] & E. Restrepo-Parra[1]

[1] Universidad Nacional de Colombia Sede Manizales, Laboratorio de Física del Plasma, PCM Computational Applications, Manizales, Colombia

[2] Universidad Nacional de Colombia Sede Manizales, Grupo de Propiedades térmicas, dieléctricas de compositos, Manizales, Colombia

Correspondence: E. Restrepo-Parra, Departamento de Física y Química, Universidad Nacional de Colombia, Manizales, Caldas, Colombia. Tel/Fax: 57-6887-9495. E-mail: erestrepopa@unal.edu.com

Received: Sep. 22, 2018 Accepted: October 9, 2018 Online Published: November 19, 2018

doi:10.5539/mas.v12n12p174 URL: https://doi.org/10.5539/mas.v12n12p174

Abstract

$La_{0.5}Ca_{0.5}Mn_{0.5}Fe_{0.5}O_3$ was synthesized using the solid state reaction method. This method consists of two main processes: a milling process and a subsequent thermal treatment. Two samples at different conditions were produced: one using 2 h of milling time and 900°C (M-I), and the other using 6 h of milling time and 1200°C of thermal treatment (M-II). X-ray diffraction analysis indicated, in both cases, an orthorhombic crystalline ordering of the space group Pbnm. For the case of M-I, the material exhibited secondary phases, different than the desired phase; on the contrary, in M-II, these secondary phases were not present.

The dielectric response determined using electrochemical impedance spectroscopy (EIS) performed in a temperature range between 20°C and 300°C exhibited a thermally activated semiconductor behavior with activation energies of E_g= 0.11±0.05 eV and E_g= 0.47±0.06 eV for M-I and M-II, respectively.

Keywords: Perovskite, solid state, conductivity, Impedance spectroscopy, gap energy

1. Introduction

Transition metal doped oxides have been a subject of interest since the 1950s because of their unique electrical, magnetic and structural properties (Jonker & Van Santen, 1950). In particular, manganite materials with the general formula ABO_3, where A is a trivalent rare-earth ion, such as La^{3+}, Pr^{3+}, and Nd^{3+}, or a divalent alkaline earth ion, such as Ca^{2+}, Sr^{2+}, Ba^{2+}, etc., have been widely studied (Gómez, Chavarriaga, Supelano, Parra, & Morán, 2018; Jonker & Van Santen, 1950). Depending on the ions included, there is a drastic difference in the physical properties of these materials, as structural, morphological, electrical and magnetic properties (Elghoul, Krichene, Boudjada, & Boujelben, 2018; Elghoul, Krichene, & Boujelben, 2016). More specifically, much attention has been attracted to the properties of $La_{1-x}Ca_xMnO_3$ and related compounds, especially because of the presence of the unique phenomena of colossal magnetoresistance and the metal–insulator transition (Restrepo-Parra, Salazar-Enríquez, Londoño-Navarro, Jurado, & Restrepo, 2011). These compounds have been analyzed since the early days of manganite studies, motivated by the double exchange (DE) mechanism between Mn^{3+}–O–Mn^{4+} (Restrepo-Parra, Bedoya-Hincapié, Jurado, Riano-Rojas, & Restrepo, 2010). Due to the presence of Mn^{3+} and Mn^{4+} ions, and depending on the degree of doping at a particular range, an insulator–metal transition (T_{IM}) accompanied by a paramagnetic–ferromagnetic transition has been observed. When the B-site is occupied by a transition metal ion such as Fe, with nearly similar ionic size to the manganese ions, the changes in the physical properties (basically electrical conduction and ferromagnetic coupling) can be explained in terms of double-exchange (Zener, 1951) and electron-phonon coupling mechanisms. The latter mechanism gives rise to B-sites becoming structurally distorted, i.e., so-called Jahn–Teller (JT) distortions, which leads to a higher localization of the charge carriers, resulting in an increase in the resistivity that is strongly dependent on the doping concentration (Kumar, Kishan, Rao, & Awana, 2010). An important manganite with the condition mentioned above is $La_{1-y}Ca_yMn_{1-x}Fe_xO_3$ (LCMFO). Some studies in this direction have been addressed, and doping effects arising, for instance, from Fe for Mn in $La_{0.7}Ca_{0.3}MnO_3$ have been reported with an elevated resistivity ascribed to a reduced hole concentration (when Mn^{4+} ion is replaced), as well as to a reduced number of mobile e_g electrons (when Mn^{3+} ion is replaced) in the fractional concentration range of 0-0.12 for Fe (Sun, Rao, Shen, & Wong, 1998). It is remarkable that both Fe^{+3}

and Mn^{3+} ions in the high spin (HS) state have an identical effective ionic radius (0.645 Å) (Shannon, 1976). As a result, the strong lattice effects can be bypassed, and therefore, the effects due to changes in the electronic structure become evident (Abdel-Khalek, EL-Meligy, Mohamed, Amer, & Sallam, 2009; Ulyanov et al., 2007). These compounds exhibit strong changes on charge ordering and the double exchange interaction. The substitution of Mn^{3+} ions by Fe^{3+} ions in LCMFO entails the generation of Fe^{3+}-Mn^{4+} sets, which eliminates the DE interaction between Mn ions and the corresponding ferromagnetic interaction, decreasing the transition temperature and increasing in resistivity. Moreover, an interesting behavior has been found LCMFO, like a great decrease in the electrical resistivity caused by an external magnetic field at around the critical temperature. Furthermore, as the Fe doping is increased, the JT effect and lattice distortion entail an additional holes localization(Dang et al., 2018; Shokr & Hussein, 2018). Moreover, the authors of this last reference affirm that with Fe doping, the available hopping sites are suppressed, and for x>0.08, the compound behaves as an insulator. However, in that study, the maximum composition achieved was x=0.30, and no higher concentrations were explored. In this study, we focus on the electronic and magnetic properties of this system for a sufficiently high concentration of x=0.5, where we assume that important changes and differences with respect to the same system in the doping regime at lower concentrations can be obtained. In addition, note that one of the most important applications of these materials is as a cathode in Solid Oxide Fuel Cells (SOFCs). Previous results have demonstrated that SOFCs could become promising devices for power generation because of the high energy conversion efficiency, negligible environmental pollution and the possibility of using carbon-based fuels (ZHAO, LI, KONG, WU, & MA, 2011). Nevertheless, the high operating temperature of approximately 1000°C for SOFCs leads to some problems in the device performance. For example, Jie et al. (ZHAO et al., 2011) developed novel cathode materials of $La_{1-x}Ca_xFe_{0.9}Mn_{0.1}O_3$ using the solid-state reaction method, with high performance for intermediate temperatures between 300°C and 850°C, resulting in activation energies of 0.2404 eV and 0.2426 eV, respectively; however, they did not perform an analysis at lower temperatures, including room temperature. Furthermore, the stoichiometry of $La_{0.5}Ca_{0.5}Fe_{0.5}Mn_{0.5}O_3$ has not been widely studied.

The aim of this work is therefore to produce $La_{0.5}Ca_{0.5}Mn_{0.5}Fe_{0.5}O_3$ using the solid state route, which could be useful for future applications in electrodes of SOFCs. Fe ions and Mn ions are both magnetic. The influence of the route of materials production on the structural and electrical properties was analyzed.

2. Experimental Details

From the precursors La_2O_3, CaO_2, Fe_2O_3 and MnO_2 (Panreac Química SLU trading house, 99.9% purity), the stoichiometric proportions were weighted in the following manner according to the desirable nominal stoichiometry: La_2O_3 40.727 gr, CaO_2 18.020 gr, Fe_2O_3 19.962 gr and MnO_2 21.735 gr, for both M-I and M-II samples. The powders of the M-I and M-II samples were mixed and then milled in a planetary ball mill for 2 h and 12 h, respectively. Two different calcination processes were performed, one at 900°C for 2 h (M-I) and the other one at a temperature of 1200°C for 6 h (M-II). All procedures were performed under air atmosphere at atmospheric pressure.

The crystalline structure of the two samples was determined from X-ray diffraction at 300 K using Cu-Kα (λ=1.5406 Å) radiation over the scan range of $20° < 2\theta < 80°$, with steps of 2 deg/min.

The electrical conductivity was determined from measurements of the impedance, $Z^*(\omega) = Z_{Re}(\omega) - iZ_{Im}(\omega)$ ($\omega = 2\pi f$ [Hz]). The analysis of the materials with impedances up to 100 MΩ was performed over a frequency range between 10 μHz and 32 MHz with a dielectric interface using SOLARTRON 1296 equipment. For impedances up to 100 TΩ, a frequency range between 10 MHz and 10 μHz was examined using a two-electrode configuration (platinum). The excitation signal was 500 mV in air atmosphere. A K-type thermocouple located in a region very close to the sample was used as a temperature sensor. The temperature range was between 25°C and 300°C.

3. Results and Discussion

3.1 X-Ray Diffraction

Figure 1 shows X-ray diffraction analysis of samples M-I and M-II at room temperature. These results reveal the occurrence of a perovskite structure for both samples. The main difference lies in the fact that for M-I peaks, associations with the initial precursors are still observed, in contrast to the results observed for M-II. Rietveld analysis was performed using the GSAS & EXPGUI software (Toby, 2001). Based on the analysis, an orthorhombic crystalline structure and symmetry space group Pbnm were assigned.

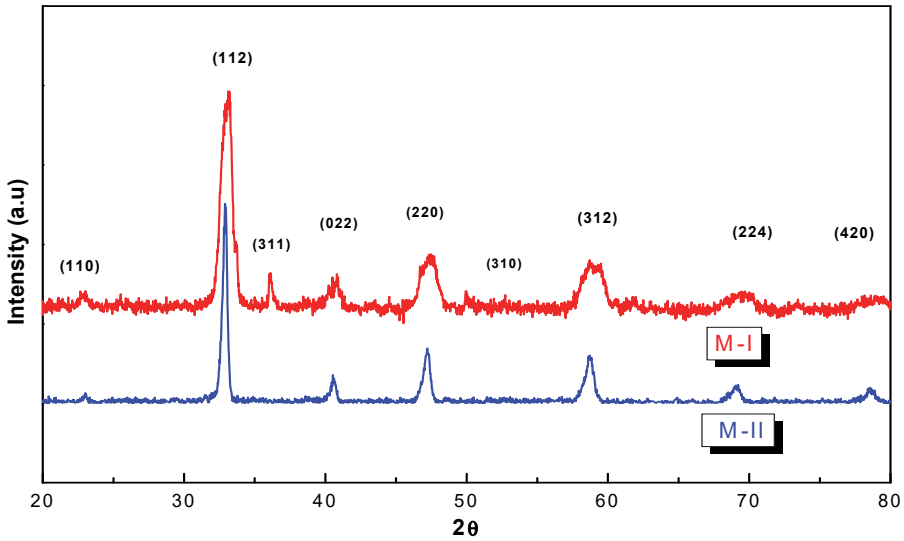

Figure 1. Room temperature X-ray diffractograms for M-I and M-II samples.

Table 1 presents the lattice parameters for M-I and M-II. These values of the lattice parameters are similar to those reported by E.A. Mohamed (Mohamed, 2012). A small broadening that is observed is attributed to the substitution of Mn^{3+} by Fe^{3+}, which can occur because both Mn^{3+} and Fe^{3+} exhibit similar sizes and ionic radii (0.0654 nm). Many researchers have reported appreciable changes caused by the Fe doping in this type of manganite (Ahn, Wu, Liu, & Chien, 1996; Tong, Zhang, Tan, & Zhang, 2004).

Table 1. Lattice parameters for both samples, M-I and M-II.

Sample	*a* (Å)	*b* (Å)	*c* (Å)	Crystallite size (nm)
M-I	5.381275±0.0004	7.639174±0.0004	5.472738±0.0004	249.765
M-II	5.465889±0.0004	7.634212±0.0004	4.447900±0.0004	848.2

For M-I, the plane (311) orientation corresponding to the $Fe_2Mn_1O_4$ phase (Varshney & Yogi, 2011) can be identified; next, to avoid formation of undesirable phases, increased milling and thermal treatment times were required. Considering this request, M-II was produced. In Figure 1, the diffractogram belonging to this sample does not exhibit the existence of peaks belonging to the chemical precursors or the undesirable phases; this result indicates a better substitution of Mn^{3+} by Fe^{3+}; otherwise, in the diffractogram corresponding to the M-II, better defined peaks were observed with lower broadening, indicating higher crystallinity. Similar results were presented by Mohamed [12] for $La_{0.5}Ca_{0.95}Mn_{0.05}Fe_{0.5}O_{3+\delta}$ and reported a small difference in the stoichiometry compared with the materials analyzed in our work. This author reported lattice parameter values of a=5.412 Å, b=5.372 Å and c=7.594 Å, Pbnm. Kumar et al. (Kumar et al., 2010) presented similar results for $La_{0.7}Ca_{0.3}Mn_{0.5}Fe_{0.5}O_3$, obtaining lattice parameter values of a=5.474 Å, b=5.482 Å, and c=7.738 Å, with space group Pbnm.

Thermal treatment and the milling process result in the substitution of Mn^{3+} by Fe^{3+}. According to the obtained results, it can be concluded that this method is suitable for the production of these perovskite materials because these processes produce bond breaking due to different phenomena, such as the vibration of the crystalline structure atoms belonging to the chemical precursors that provides sufficient energy for generating new bonds. Atoms from the precursors can be moved, leading to stronger and more stable bonds. As a result, materials with new physical and chemical properties different from those of the precursors are obtained, as is shown in the materials characterization. Table 1 also presents the crystallite size for both M-I and M-II samples. M-II exhibits a larger crystallite size than M-I. With increasing temperature, the grain size increased and the crystallites become rearranged into a more stable state (Abdoli, Ghanbari, & Baghshahi, 2011).

3.2 Impedance Spectroscopy

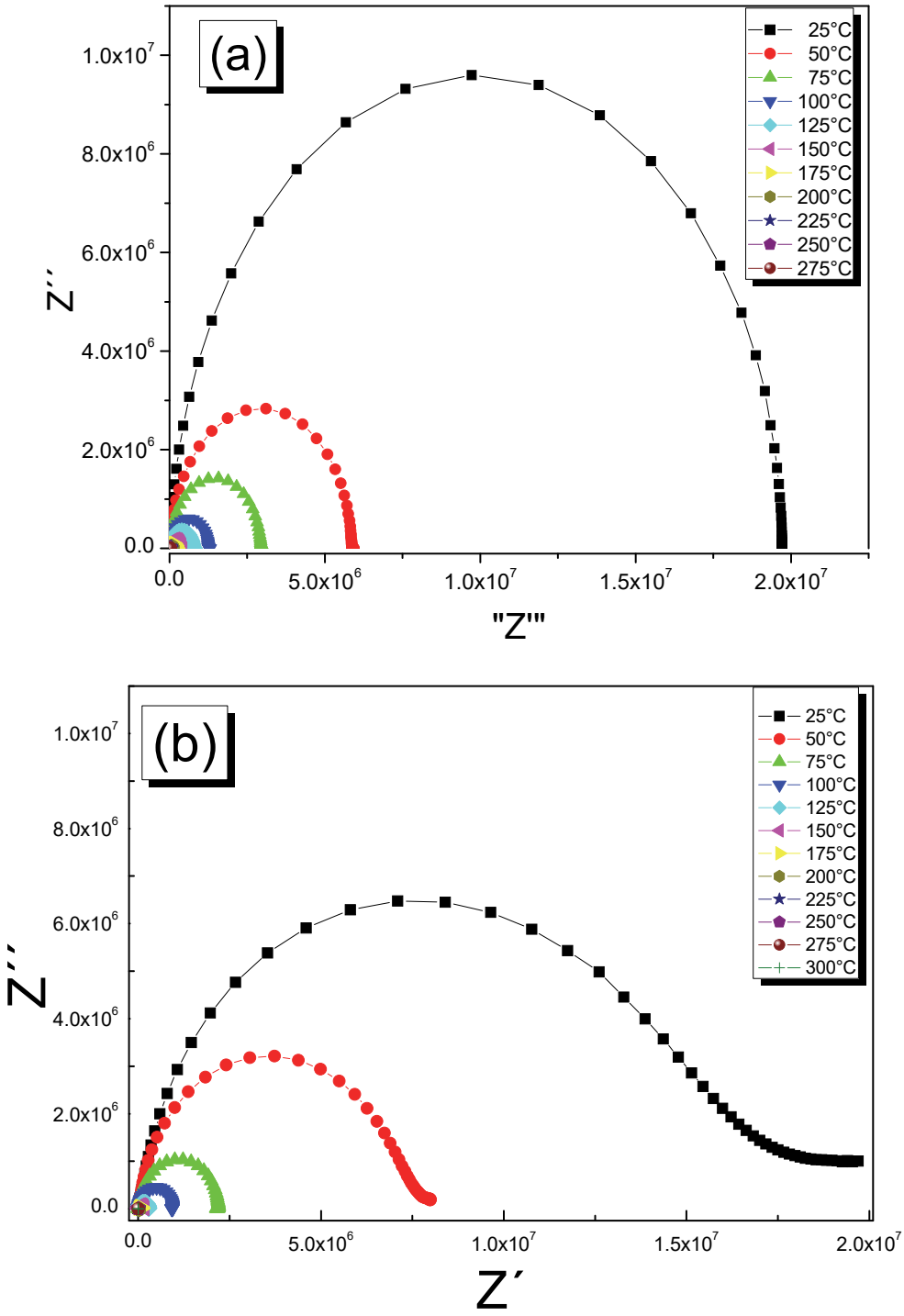

Figure 2. Nyquist diagrams for samples (a) M-I and (b) M-II.

EIS analysis (Figure 2) shows Nyquist diagrams for different temperatures. The EIS technique forms a good diagnostic tool for evaluating performance owing to its ability to separate the impedance responses of the various transport processes occurring simultaneously (Li & Pickup, 2003). This is a powerful technique that allows to reach a greater understanding of the electrical properties. The radius of semicircles decreases as the temperature decreases, that means a decrease in the resistivity. This technique is complemented with an electrical circuit that allows to model the electrical behavior of the materials. This electrical circuit can be considered as the best

representation of the relationship between real and imaginary impedances. The circuit is composed by an *Rg* resistance that represents the response of the grains, that is placed in series with a circuit (*Rgb*/*CPEgb*) which referes to the response of grain boundaries, being *Rgb* and *CPEgb* the grain boundary resistance and capacitance, respectively (Ncib et al., 2018).

Generally, the high-frequency region (>100 Hz) of an impedance spectrum reflects the charge transport, whereas the low-frequency region (around 50.01 Hz,) represent mass transport. The relative importance of the transport processes depends on the steady-state value of the overpotential at which the EIS experiment is conducted. At low overpotentials when the mass transport resistance is not significant, the main contributor to the impedance is the charge transport. At moderate overpotentials mass transport begins to contribute to the total impedance of the cell (Gomadam & Weidner, n.d.). In our case, the EIS diagrams plotted in the Nyquist plane show the classical aspect for a redox system: a semi-circle corresponding to the charge transfer process (charge transfer resistance in parallel to the double layer capacitance); because of the low value of the overpotential used in the EIS experiment (100 mV), the main contributor to the impedance is the charge transport. On the other hand, there is a difference between the results for both M-I and M-II samples. In fig. 2(a), for M-I, the Nyquist plots consist of an out-of-shaped semicircle alike in appearance of a half ellipse. On the other hand, fig. 2(b), for M-II, the Nyquist plots are more similar to a semicircle in high and intermediate frequency ranges and a straight line in the lower frequency range. To compare with that for M-I, the semicircles for M-II are much smaller. In our work, the high frequency semicircles increase obviously with the decrease of temperature. From these results, the conductivity was obtained using the following expression:

$$\sigma_{dc} = \frac{RA}{d} \tag{1}$$

where R is the material volumetric resistance (bulk resistance), A is the cross section of the sample, and d is the material thickness. In the plot of $log(\sigma)$ versus $1000/T$ (Figure 3), an Arrhenius type tendency was observed, which can be described as follows:

$$\sigma(T) = \sigma_0 e^{(E_g/k_b T)} \tag{2}$$

where k_b is the Boltzmann constant, T is the absolute temperature, and σ_0 is the pre-exponential factor (for M-I: $e^{1.19}$, for M-II: $e^{0.5776}$). From these results, it is possible to conclude that the conduction is thermally activated, with activation energies (E_a) of 0.23 ± 0.07 eV and 0.11 ± 0.05 eV for M-I and M-II, respectively. Jie et al. (ZHAO et al., 2011) reported activation energies of 0.2404 eV and 0.1147 eV. These activation energies are also associated with polaron energy hopping, due to the interaction between electrons and ions in the crystalline lattice via coulomb interactions. Conductivity values of 4.45×10^{-5} S-cm^{-1} and 3.74×10^{-4} S-cm^{-1} were obtained for M-I and M-II, respectively.

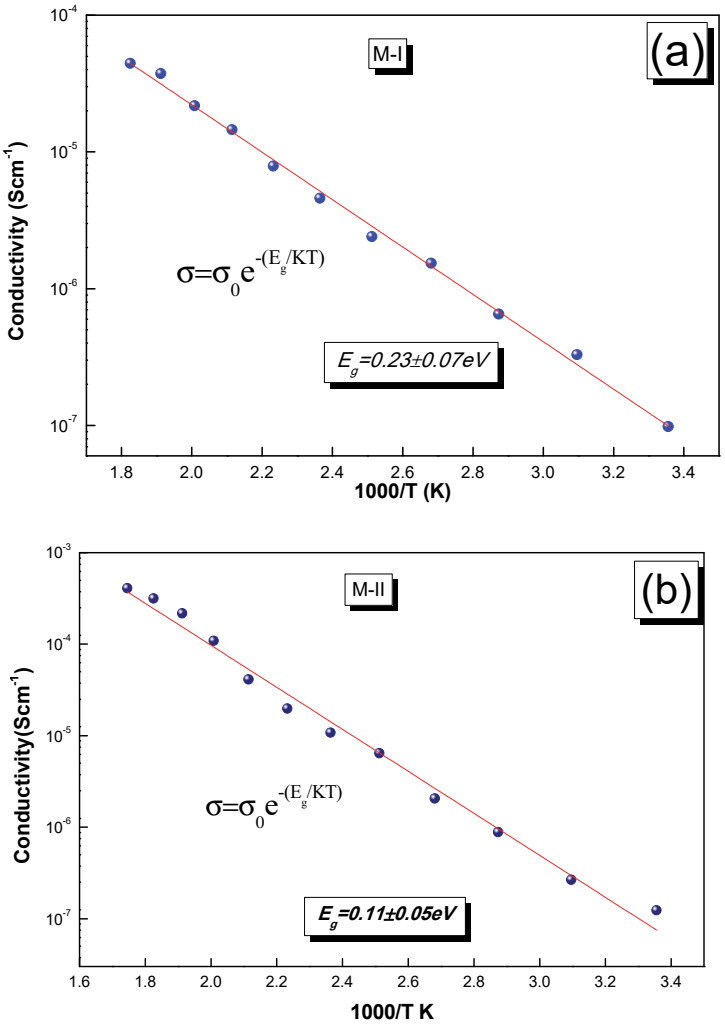

Figure 3. Arrhenius type DC conductivity as a function of the temperature obtained from the EIS analysis. Solid lines represent a linear fit used to determine the activation energies.

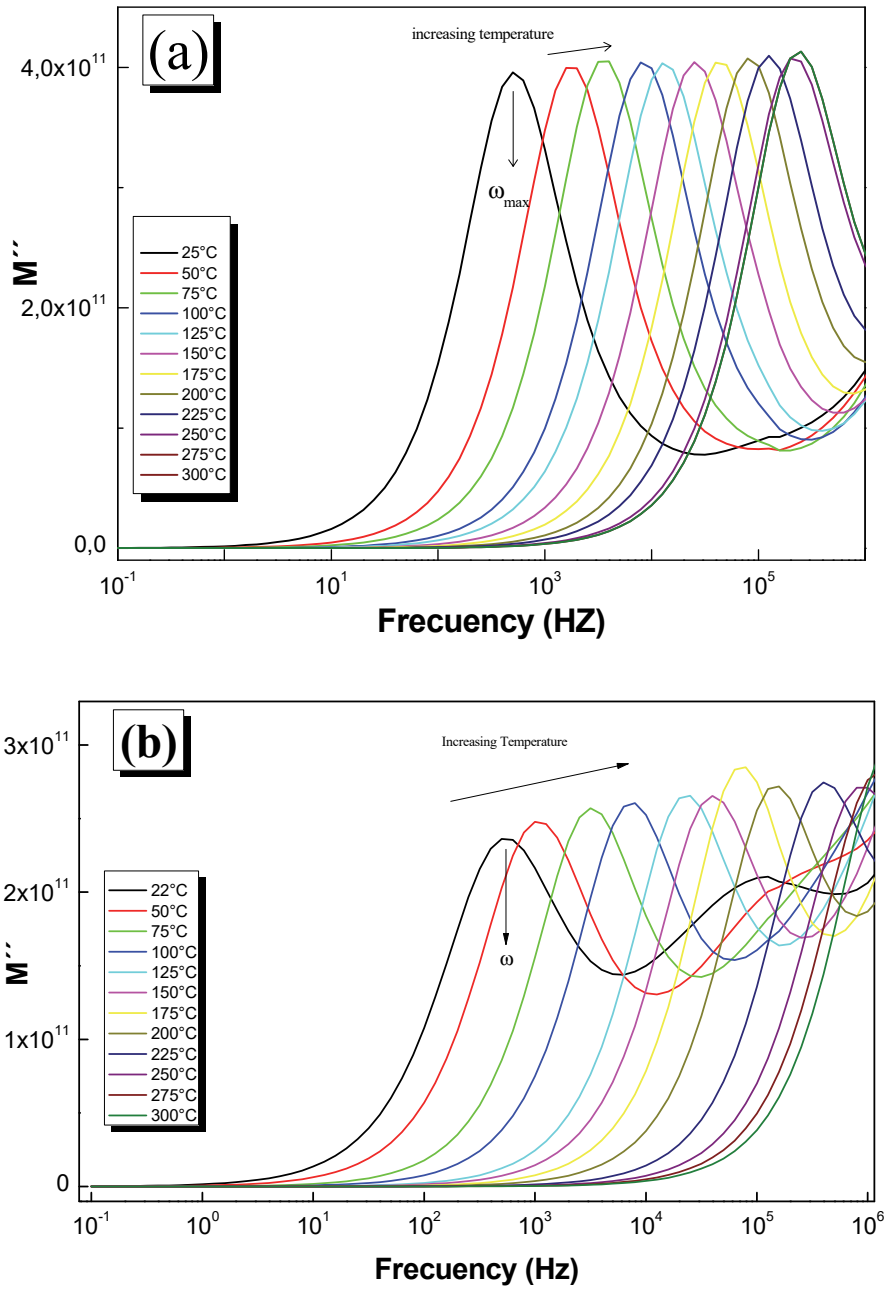

Figure 4. Imaginary part of the dielectric moduli as a function of the frequency for several temperatures for (a) M-I and (b) M-II.

In the case of the complex dielectric modulus, $M^*(\omega)$, the variation of the imaginary part M'' versus frequency at several temperatures is presented in Figure 4. The curves exhibit maxima that are shifted toward greater frequencies as the temperature is increased. The symmetry of the peaks that are moved away from the ideal values (one) is indicative that there is a time relaxation distribution in the conduction process and that this distribution is moved away from the Debye-type model. Based on the maximum position, M''_{max}, the relaxation time (τ) was determined using the expression $\omega_{max}\tau = 1$. The τ variation as a function of the temperature is shown in Figure 4, according to the expression.

$$\omega_{max} = \omega_0 e^{(-E_{\omega\, max})/k_b T} \quad \text{or} \quad ln(\omega_{max}) = (\omega_0 - E_{\omega\, max})/k_b T \qquad (3)$$

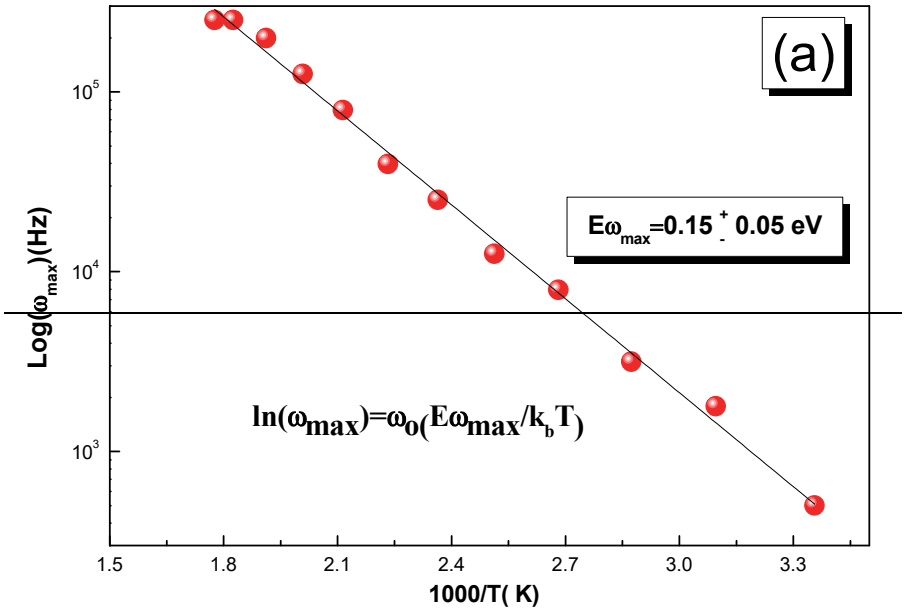
(a)
$E\omega_{max}$=0.15 $^{+}_{-}$ 0.05 eV
$\ln(\omega_{max})=\omega_0(E\omega_{max}/k_bT)$
Log(ω_{max})(Hz)
10^5
10^4
10^3
1.5 1.8 2.1 2.4 2.7 3.0 3.3
1000/T(K)

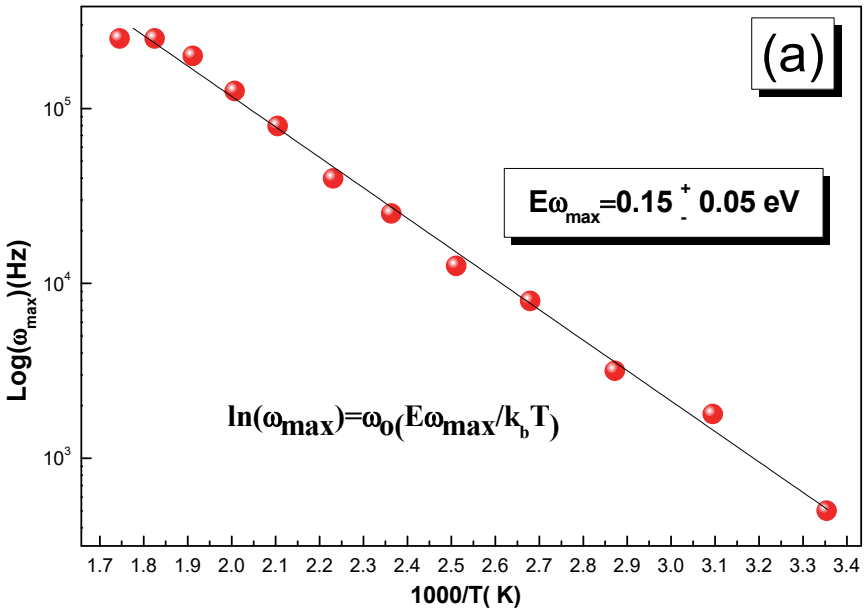
(a)
$E\omega_{max}$=0.15 $^{+}_{-}$ 0.05 eV
$\ln(\omega_{max})=\omega_0(E\omega_{max}/k_bT)$
Log(ω_{max})(Hz)
10^5
10^4
10^3
1.7 1.8 1.9 2.0 2.1 2.2 2.3 2.4 2.5 2.6 2.7 2.8 2.9 3.0 3.1 3.2 3.3 3.4
1000/T(K)

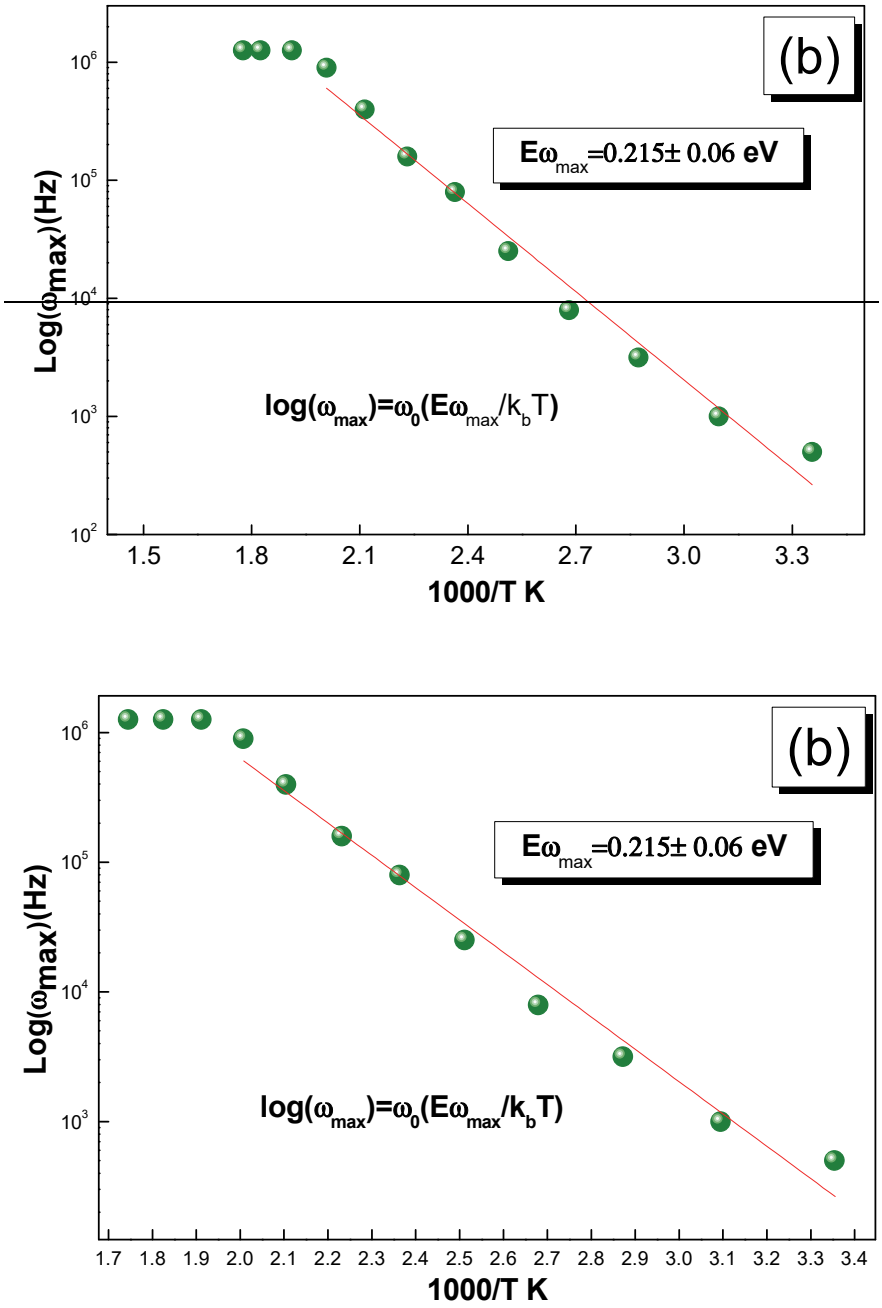

Figure 5. Arrhenius type behavior of the ω_p maximum values (according to Figure 4). The solid line represents the better linear fit for determining E_g.

The Arrhenius-type tendency in the insolated phase indicates a thermally activated process, where ω_{max} is the maximum value of carrier hopping frequency, generating activated energies of E_g=0.16±0.06 eV and E_g=0.215±0.06 eV for M-I and M-II, respectively, as shown in Figure 5. This behavior provides evidence that in the carriers hopping process, an intrinsic mechanism prevails over any other and that the relaxation times are affected by bulk effects. we can see, in figure 4 (b), that the mechanism of relaxation produces a second peak, at room temperature (22 °C). This peak associated to the infrared frequency of 10^5 (Hz).

4. Conclusions

$La_{0.5}Ca_{0.5}Fe_{0.5}Mn_{0.5}O_3$ compounds were produced in bulk using the solid-state reaction method under two conditions of milling and thermal treatment time (M-I and M-II). The structural changes observed in M-II were caused by the change in the production conditions. These structural changes are especially reflected in the

elimination of secondary phases and the increase in the crystallite size.

DC conductivity obtained by EIS analysis indicated a thermally activated behavior. The activation energies for these materials exhibited values of 0.23 ± 0.07 eV and 0.11 ± 0.05 eV, which are similar to those reported for other doped manganites, and the particule size improves the transport of electrons through the lattice, because the big and homogenenous grains, with small grain boundaries are better conductor.

Acknowledgments

The authors gratefully acknowledge the financial support of Facultad de Ciencias Exactas y Naturales of the Universidad Nacional de Colombia sede Manizales, La Dirección Nacional de Investigaciones de la Universidad Nacional de Colombia sede Manizales DIMA, and Departamento Administrativo de Ciencia, Tecnología e Innovación (**Colciencias**).

References

Abdel-Khalek, E. K., EL-Meligy, W. M., Mohamed, E. A., Amer, T. Z., & Sallam, H. A. (2009). Study of the relationship between electrical and magnetic properties and Jahn–Teller distortion in R0.7Ca0.3Mn0.95 Fe0.05O3 perovskites. *Journal of Physics: Condensed Matter*, *21*(2), 26003. Retrieved from http://stacks.iop.org/0953-8984/21/i=2/a=026003

Abdoli, H., Ghanbari, M., & Baghshahi, S. (2011). Thermal stability of nanostructured aluminum powder synthesized by high-energy milling. *Materials Science and Engineering: A*, *528*(22), 6702–6707. https://doi.org/https://doi.org/10.1016/j.msea.2011.05.057

Ahn, K. H., Wu, X. W., Liu, K., & Chien, C. L. (1996). Magnetic properties and colossal magnetoresistance of La(Ca)MnO3 materials doped with Fe. *Phys. Rev. B*, *54*(21), 15299–15302. https://doi.org/10.1103/PhysRevB.54.15299

Dang, N. T., Zakhvalinskii, V. S., Kozlenko, D. P., Phan, T.-L., Kichanov, S. E., Trukhanov, S. V, … Trukhanova, E. L. (2018). Effect of Fe doping on structure, magnetic and electrical properties La0.7Ca0.3Mn0.5Fe0.5O3 manganite. *Ceramics International*, *44*(13), 14974–14979. https://doi.org/https://doi.org/10.1016/j.ceramint.2018.05.124

Elghoul, A., Krichene, A., Boudjada, N. C., & Boujelben, W. (2018). Rare earth effect on the critical behavior of La0.75Ln0.05Sr0.2MnO3 manganites. *Ceramics International*, *44*(12), 14510–14517. https://doi.org/https://doi.org/10.1016/j.ceramint.2018.05.066

Elghoul, A., Krichene, A., & Boujelben, W. (2016). Electrical, magnetic and magnetocaloric properties of polycrystalline Pr0.63A0.07Sr0.3MnO3 (A=Pr, Sm and Bi). *Journal of Physics and Chemistry of Solids*, *98*, 263–270. https://doi.org/https://doi.org/10.1016/j.jpcs.2016.07.021

Gomadam, P. M., & Weidner, J. W. (n.d.). Analysis of electrochemical impedance spectroscopy in proton exchange membrane fuel cells. *International Journal of Energy Research*, *29*(12), 1133–1151. https://doi.org/10.1002/er.1144

Gómez, A., Chavarriaga, E., Supelano, I., Parra, C. A., & Morán, O. (2018). Tuning the magnetocaloric properties of La0.7Ca0.3MnO3 manganites through Ni-doping. *Physics Letters A*, *382*, 911–919. https://doi.org/10.1016/j.physleta.2018.01.030

Jonker, G. H., & Van Santen, J. H. (1950). Ferromagnetic compounds of manganese with perovskite structure. *Physica*, *16*, 337–349. https://doi.org/10.1016/0031-8914(50)90033-4

Kumar, N., Kishan, H., Rao, A., & Awana, V. P. S. (2010). Fe ion doping effect on electrical and magnetic properties of La0.7Ca0.3Mn1−xFexO3 (0≤x≤1). *Journal of Alloys and Compounds*, *502*(2), 283–288. https://doi.org/https://doi.org/10.1016/j.jallcom.2010.04.187

Li, G., & Pickup, P. G. (2003). Ionic Conductivity of PEMFC Electrodes: Effect of Nafion Loading. *Journal of The Electrochemical Society*, *150*(11), C745–C752. https://doi.org/10.1149/1.1611493

Mohamed, E. A. (2012). Structural and electrical properties of La0.5Ca0.5Mn0.95Fe0.05O3δ perovskite. *Journal of Alloys and Compounds*, *543*, 40–42. https://doi.org/https://doi.org/10.1016/j.jallcom.2012.07.120

Ncib, W., Kharrat, A. B. J., Wederni, M. A., Chniba-Boudjada, N., Khirouni, K., & Boujelben, W. (2018). Investigation of structural, electrical and dielectric properties of sol-gel prepared La0.67-xEuxBa0.33Mn0.85Fe0.15O3 (x=0.0, 0.1) manganites. *Journal of Alloys and Compounds*, *768*, 249–262. https://doi.org/https://doi.org/10.1016/j.jallcom.2018.07.192

Restrepo-Parra, E., Bedoya-Hincapié, C. M., Jurado, F. J., Riano-Rojas, J. C., & Restrepo, J. (2010). Monte Carlo study of the critical behavior and magnetic properties of La2/3Ca1/3MnO3 thin films. *Journal of Magnetism and Magnetic Materials*, *322*(21), 3514–3518. https://doi.org/https://doi.org/10.1016/j.jmmm.2010.06.055

Restrepo-Parra, E., Salazar-Enríquez, C. D., Londoño-Navarro, J., Jurado, J. F., & Restrepo, J. (2011). Magnetic phase diagram simulation of La1−xCaxMnO3 system by using Monte Carlo, Metropolis algorithm and Heisenberg model. *Journal of Magnetism and Magnetic Materials*, *323*(11), 1477–1483. https://doi.org/https://doi.org/10.1016/j.jmmm.2011.01.003

Shannon, R. D. (1976). Revised effective ionic radii and systematic studies of interatomic distances in halides and chalcogenides. *Acta Crystallographica Section A*, *32*(5), 751–767. https://doi.org/10.1107/S0567739476001551

Shokr, F. S., & Hussein, M. (2018). Physical properties of La0.67Ca0.13Sr0.2Mn1−xFexO3 compounds doped Fe. *Results in Physics*, *8*, 186–189. https://doi.org/https://doi.org/10.1016/j.rinp.2017.11.005

Sun, J. R., Rao, G. H., Shen, B. G., & Wong, H. K. (1998). Doping effects arising from Fe and Ge for Mn in La0.7Ca0.3MnO3. *Applied Physics Letters*, *73*(20), 2998–3000. https://doi.org/10.1063/1.122656

Toby, B. H. (2001). EXPGUI, a graphical user interface for GSAS. *Journal of Applied Crystallography*, *34*(2), 210–213. https://doi.org/10.1107/S0021889801002242

Tong, W., Zhang, B., Tan, S., & Zhang, Y. (2004). Probability of double exchange between Mn and Fe in LaMn1-xFexO3. *Phys. Rev. B*, *70*(1), 14422. https://doi.org/10.1103/PhysRevB.70.014422

Ulyanov, A. N., Kim, J. S., Shin, G. M., Song, K. J., Kang, Y. M., & Yoo, S. I. (2007). La0.7Ca0.3Mn0.95M0.05O3 manganites (M=Al, Ga, Fe, Mn, and In): Local structure and electron configuration effect on Curie temperature and magnetization. *Physica B: Condensed Matter*, *388*(1), 16–19. https://doi.org/https://doi.org/10.1016/j.physb.2006.04.033

Varshney, D., & Yogi, A. (2011). Structural and transport properties of stoichiometric Mn2+-doped magnetite: Fe3−xMnxO4. *Materials Chemistry and Physics*, *128*(3), 489–494. https://doi.org/https://doi.org/10.1016/j.matchemphys.2011.03.040

Zener, C. (1951). Interaction between the d-Shells in the Transition Metals. II. Ferromagnetic Compounds of Manganese with Perovskite Structure. *Phys. Rev.*, *82*(3), 403–405. https://doi.org/10.1103/PhysRev.82.403

ZHAO, J., LI, C., KONG, L., WU, X., & MA, Y. (2011). Synthesis and characterization of calcium and manganese-doped rare earth oxide La1-xCaxFe0.9Mn0.1O3-δ for cathode material in IT-SOFC. *Journal of Rare Earths*, *29*(11), 1066–1069. https://doi.org/https://doi.org/10.1016/S1002-0721(10)60599-6